Structural transitions during Ni nanoparticle formation by decomposition of a Ni-containing metal-organic framework using *in-situ* total scattering

Nils Prinz[1], Sven Strübbe[2], Matthias Bauer[2], Mirijam Zobel[1,*]

[1] *Institute of Crystallography, RWTH Aachen University, 52066 Aachen, Germany*

[2] *Department of Chemistry and Center for Sustainable Systems Design, Paderborn University, 33098 Paderborn, Germany*

Abstract

For improved and rational design of catalysts, in-depth knowledge of their formation and structural evolution during synthesis is a key parameter. Thus, preparation of a Ni methanation catalyst derived from a Ni-containing metal-organic framework Ni(BDC)(PNO) under different gas atmospheres (He vs. 10 % H_2/He) and temperatures (342°C, 375 °C, 411 °C, 500 °C) was studied thoroughly using *in-situ* pair distribution function analysis, X-ray absorption spectroscopy and thermogravimetric analysis. Framework decomposition is initiated by a distortion of the MOF framework structure, followed by the release of trapped solvent molecules. Then, the pyridine-*N*-oxide (PNO) linker is released from the framework, followed by the benzenedicarboxylate linker, leading to the collapse of the framework and the formation of 2 nm nickel nanoparticles surrounded by a carbon shell, that grow to 4 nm under further heating. Without reducing atmosphere, carbon is intercalated into the Ni structure forming a Ni_{hcp} side phase, which is inactive in the methanation reaction.

Introduction

Metal-organic frameworks (MOFs) feature well-defined crystallinity and the possibility to tailor their composition and porosity. Employing mixed metals and designed linkers, MOFs can be tuned to achieve different desired properties. This makes them exceptional and structurally highly defined precursors to form nanostructured catalysts by treatment in controlled atmospheres.[1,2] Various synthetic approaches exist to convert MOF precursors to functional materials with thermal treatment, such as pyrolysis,[3,4] MOF-templated strategies[5–7], chemical vapour deposition[8], electrospinning[9] and impregnation methods.[10] Variation of the thermal treatment conditions yields a broad spectrum of catalysts with different porosity,[11] compositions like mixed oxidation states of the metal ions[12] and morphologies like cubes or platelets.[13,14] During the thermal treatment, the organic linkers are decomposed to form porous carbon or volatile oxidized organic species, such as CO_2, and the metal ions transition to metal or metaloxide nanoparticles.[15–17] The organic and metal decomposition products are dependent on the atmosphere during thermal treatment. In oder to optimize thermal treatment conditions, i.e. gas atmosphere, pressure, temperature and heating ramp, *in-situ* structural studies during formation of the nanostructured materials are of great value. Most

studies on MOF-derived nanostructured materials focus on the synthetic procedures and their catalytic applications, as well as on the characterization of the final products. For various catalytic reactions, like the CO_2 methanation, Fischer-Tropsch synthesis (FTS) and the oxygen evolution reaction, MOF-derived catalysts have been synthesized [18–20], and the performance of the resulting methanation and FTS catalysts has even surpassed commercial catalysts.

In a previous work, we highlighted the application of a MOF-derived Ni@C catalyst for the methanation of CO_2, which featured Ni nanoparticles stabilized by a carbon shell.[21] The MOF-precursor for this Ni@C catalyst is Ni(BDC)(PNO), featuring high crystallinity and high amounts of carbon per nickel atoms.[22] It contains Ni^{2+} as inorganic nodes, linked by the organic benzenedicarboxylate (BDC) and bridged via pyridine-*N*-oxide (PNO) linkers (see Figure 1). The PNO is blocking the pores of the MOF, which increases the amount of carbon and should prevent the agglomeration of the metal atoms.

In order to follow the structural reorganisation from the crystalline MOF, via possibly disordered states to nanostructured catalytically active materials, X-ray total scattering with subsequent pair distribution function (PDF) analysis is of great value. The PDF displays all real space interatomic distances in the sample and is, hence, suited to study the short- to medium-range order of amorphous and nanostructured materials together with the long-range order of crystalline materials.[23] While common powder X-ray diffraction is mainly sensitive to crystalline matter without access to disordered states of matter with the diffuse diffraction signal lying underneath and in between the Bragg peaks, PDF is highly suited to access the local structural motifs in disordered materials. Synchrotron X-ray scattering has the advantage of a very high time resolution in the (sub)-second regime thanks to high brilliance combined with 2D detectors, and high-energy X-rays can readily penetrate thick samples, making it especially suited for *in-situ* experiments.[24,25] Some studies of MOFs with *in-situ* pair distribution function (PDF) analysis exist, mainly involving structural changes during catalytic application and formation of the MOF itself.[26–28] But only few studies have been done so far, which deal with the formation of nanoparticles from MOFs during thermal treatment. For example, Folkjær *et al.* presented an *in-situ* PDF study on the formation of 10-30 nm Cu_2O and 65-80 nm Cu metal particles by thermal treatment of a Cu-containing MOF in argon atmosphere.[29] Chen *et al.* studied the nanoparticle formation from different bimetallic MOFs and demonstrated the dependence of the resulting nanoparticle structure on the node chemistry of the MOF precursor.[30] The short- to medium-range order sensitivity of PDF is nicely complemented by X-ray absorption spectroscopy (XAS).[31–33] The element specificity of this technique allows to track oxidation state changes of the metal center during thermal treatment of MOFs via X-ray absorption near edge spectroscopy (XANES).[21]

Here, we perform *in-situ* PDF experiments to study temperature-induced structural changes of Ni(BDC)(PNO) to follow the nanoparticle formation during thermal treatment, partially complemented by XANES. The temperature-dependent impact of inert and reducing gas atmospheres on the process is contrasted, and correlated with thermal gravimetric analysis (TGA) under the respective reaction conditions for mechanistic insight.

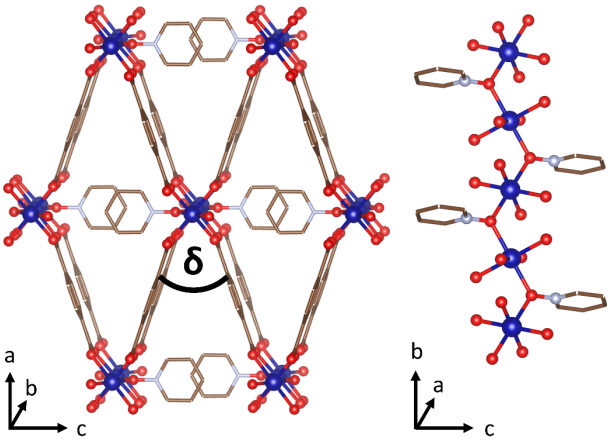

Figure 1: Structure of Ni(BDC)(PNO) MOF. Nickel in blue, oxygen in red, nitrogen in grey and the aromatic carbon linkers are simplified as brown rings. Note, that hydrogen is omitted for better visibility. On the left, the blocked pores by the pyridine-*N*-oxide are visible. The NiO_6 octahedrons are arranged in chains, with the Ni atoms bridged *via* the oxygen of the PNO, and the chains are linked by the benzenedicarboxylate (BDC) (shown on right). The BDC linker form the angle δ (left).

Experimental Section

Synthesis of Ni(BDC)(PNO)

The synthesis of Ni(BDC)(PNO) was done according to an earlier publication.[21] For this, 9.887 g (34.00 mmol) of Ni(NO3)2·6 H2O, 5.684 g (34.00 mmol) of terephthalic acid and 3.804 g (40.00 mmol) of pyridine-N-oxide were dissolved in 200 mL of dimethylformamide (DMF) in a 500 mL Schott flask using an ultrasonic bath. Subsequently, the reaction solution was heated to 120 °C for 18 h in an oven, and the resulting solid was filtered off from the hot mixture and washed with 1x100 mL DMF, 2x60 mL DMF and 1x60 mL deionized water. The solid green material was dried over night at room temperature and subsequently for 3 days at 130 °C in air. The sample investigated in this publication is from the same synthesis batch as samples in [21].

Synthesis of Ni_3C

Ni_3C was prepared by the decomposition of $Ni(acac)_2$ in oleylamine and octadecene.[34] 5.138 g (20 mmol) of $Ni(acac)_2$, 19.2 mL (60 mmol) of oleylamine and 10 mL (31 mmol) of octadecene were placed in a three-neck round bottom flask. The reaction mixture was heated up to 100 °C in Ar atmosphere and after 30 min the temperature was raised to 150 °C and held for 15 min. Finally, the temperature was raised to 200 °C and held for another 4 h. The reaction product was centrifuged at 12000 rpm and washed three times with an 1:1 acetone/hexane mixture. The black product was dried overnight at room temperature and subsequently for 3 days at 80 °C in air. The purity was confirmed with Rietveld refinement.

Thermal treatment conditions of Ni(BDC)(PNO)

We abbreviate the experiments in the style of "10H_2–342", stating first the gas atmosphere in % hydrogen and then the final temperature of the experimental run.

During the *in*-situ PDF measurements, the as-synthesized Ni(BDC)(PNO) was treated with a heat ramp of 5 °C/min and held at the final temperature 342, 375, 411, and 500 °C under 10% H2/He until no further changes appeared in the PDF measurements (180, 60, 45 and 15 min, respectively). In case of He atmosphere one experiment with the final temperature 500 °C and holding time of 60 min was conducted (see Figure 2 for visualized ramps). This means, that all experiments under 10% H_2/He are identical up to the temperature 342 °C. The resulting temperatures were calculated after calibrating the temperature inside the capillary. The observation for all experiments started at 130 °C (after applying a heat ramp of 50 °C/min), as only changes in lattice parameter occurred between 20-130 °C confirmed by PXRD and also no mass loss was observed (confirmed by TGA). Therefore, 130 °C is referenced as the time 0 min for all *in-situ* experiments.

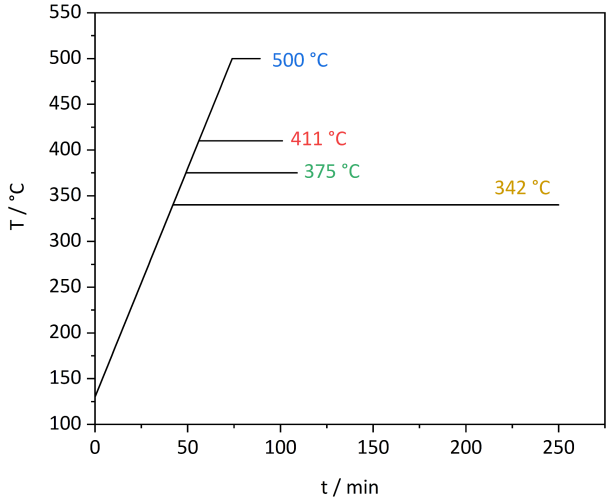

Figure 2: Temperature profiles of the thermal treatment starting at 130 °C with a heat ramp of 5 °C/min up to the respective holding temperatures.

In-situ X-ray total scattering analysis

Total scattering data was acquired at Petra III P21.1 beamline at DESY facility, Hamburg (Germany), with an X-ray energy of 102 keV (λ = 0.1215 Å) and a beamsize of 0.8x1.0 mm^2. Data was collected continuously using a Pilatus CdTe 2M detector with 10 seconds for each detector image over a Q-range of 0.5 – 25.4 $Å^{-1}$. Radial integration was done with the software xpdtools[35], PDF calculation with PDFgetX3[36] and PDF modelling with DiffPy-CMI.[37] A Si standard was measured to calibrate the detector tilt, the sample detector distance, as well as the instrumental resolution parameters Q_{damp}=0.053 and Q_{broad}=0.013.

For every experiment, 20 mg of Ni(BDC)(PNO) were filled in a capillary (1.5 mm OD, 1.48 ID) as a powder and fixed with quartz wool plugs. Prior to the experiment the apparatus was flushed with He and the O_2 concentration was controlled with an inline oxygen sensor. For heating, a hot air blower with homogeneous heating zone of about 2 mm diameter was placed under the capillary and the total gas flow of 20 mL/min was achievied by Bronkhorst mass flow controllers.

In-situ X-ray absorption spectroscopy

X-ray absorption experiments at the Ni K-edge (8333 eV) were carried out at PETRA III beamline P65 at DESY, Hamburg (Germany). The PETRA III storage ring at DESY operates at 6 GeV particle energy with a current of 120 mA in top-up mode keeping the current stable at 1%. Measurements have been performed in fluorescence mode using a Ni foil for calibration of the beam with the first inflection point of Ni K edge at 8333 eV. For beamline P65, an 11-period mini-undulator is the photon source and the incident energy is selected using a water-cooled Si (111) double crystal monochromator with a beam size of 1.0 × 0.2 mm beam spot size. The XANES analysis and the data preparation have been carried out with the program Athena of the Demeter program package.[38] For data evaluation, the spectra background has to be removed in the first instance, and, therefore, a Victoreen-type polynomial was subtracted.[39–41] The first inflection point was taken as energy E(0).

The *in-situ* XANES measurements were carried out using a self-designed cell based on MACOR ceramics. The cell was heated with heating wires and was isolated with quartz glass wool. A custom-built gas dosing system of mass flow controllers was used to control the gas flow with an overall gas flow of 100 mL/min while using a sample amount of 100 mg Ni(BDC)(PNO). Only $10H_2$-500 and He-375 with a heating ramp of 5 °C/min starting from room temperature were measured with XANES.

Thermogravimetric Analysis coupled with Mass Spectroscopy (TGA-MS)

TGA measurements were performed on a NETZSCH STA 449C Jupiter thermoanalyzer equipped with an electromagnetic microbalance with top loading. The TGA resolution was 0.1 µg and the relative error of mass determination was 0.5%. A highly sensitive sample carrier with Pt/Pt–Rh thermocouples and a controlled gas flow of 100 ml/min was used. Both gases Ar and H_2 were used with 99.999% purity. The samples were positioned into corundum crucibles (85 µl) without lids. The evolving gases during thermal treatment were monitored and analysed with a quadrupole mass spectrometer (QMS200 Omnistar, Balzers) coupled to STA *via* a quartz capillary heated to 393K. The QMS experiments are performed with an electron ionization energy of 70 eV and a dwell time per mass of 0.2s. The masses observed included 2, 12, 14, 15, 16, 17, 18, 20, 26, 27, 28, 30, 32, 39, 40, 44, 46, 50, 52, 54, 55, 65, 67, 77, 78, 79, 84, 85, 95 m/z.

Results and Discussion

Temperature-induced changes in the metal-organic framework Ni(BDC)(PNO)

The PDF of the Ni(BDC)(PNO) framework is dominated by Ni···O and Ni···Ni distances due to the stronger scattering power of Ni compared to the lighter elements H, C, N, O. Therefore, the Ni-O distance at 2.04 Å from Ni-carboxylate and Ni-pyridine-*N*-oxide interactions of the NiO_6 octahedra and the Ni···Ni distance at 3.59 Å from the corner-sharing octahedrons are most pronounced in the PDF (see Figure 3). When studying the structure of MOFs with powder X-ray diffraction (PXRD), one needs to keep in mind

that the organic linkers are rigid themselves, but have rotational freedom along the C_2 symmetry axis, due to sp^3-hybridized C-C bonds. Kolokolov *et al.* showed with solid-state ^{2}H-NMR that the activation energy for the phenylene group rotation *via* π-flipping in the comparable MIL-53 framework is 37 ± 1 kJ/mol and the aromatic ring becomes mobile at temperatures higher than 350 K.[42] With higher temperatures the π-flipping can turn into free rotation, where the aromatic ring is allowed to rotate freely along the C_2 symmetry axis.[43] Increased temperatures lead to an overall decrease in the long range order and broadening of interatomic distances (e.g at 2.04 Å representing the Ni-O distance) due to higher thermal motion of the atoms and ions, but also due to rotations of the organic linker. At a temperature of 170 °C, the peak starts to shift to lower distances with the final distance of 2.00 Å at 345 °C. This is anomalous because bond lengths should increase with temperature. The anomalous contraction of the Ni-O distance could stem from a change in ligand chemistry or due to a distortion in the framework which hinders the Ni-O distance from relaxing.

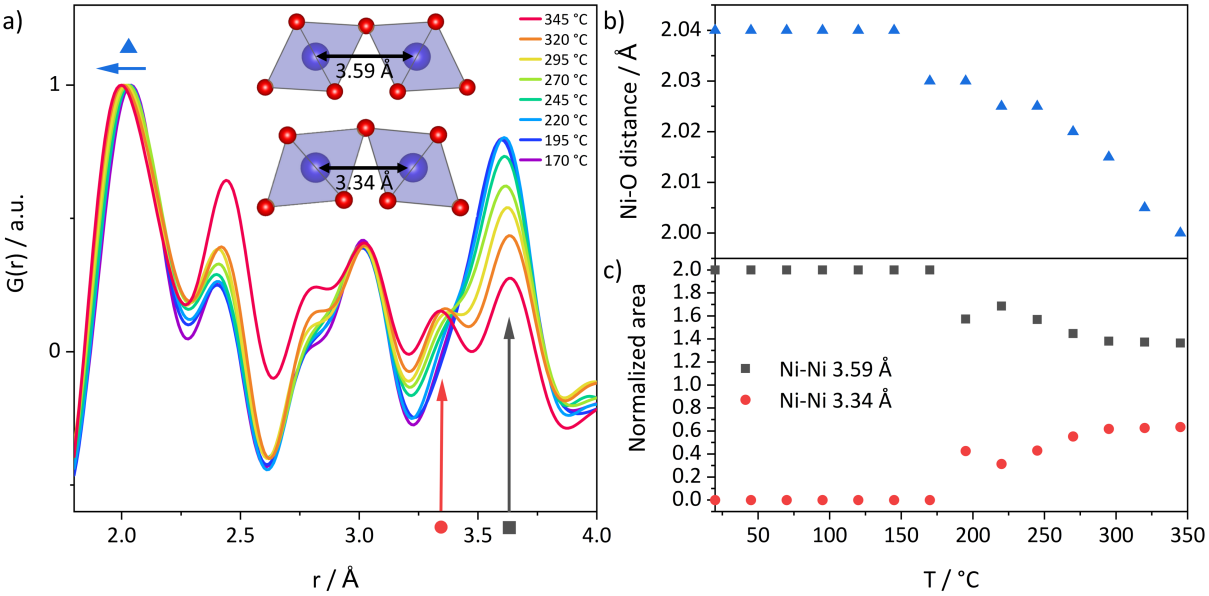

Figure 3: a) PDFs of Ni(BDC)(PNO) measured at different temperatures in He, with schematics of NiO_6 octahedra for the two Ni···Ni distances. The blue triangle shows the shift of the Ni-O distance, the red circle and black square show the two Ni-Ni distances at 3.34 and 3.59 Å, respectively. b) Corresponding changes of the Ni-O distance. c) Ratio of the peak areas of M···M distance at 3.34 and 3.59 Å.

The Ni···Ni distances of the MOF at 3.59 Å split into two peaks, beginning at around 195 °C, where the low distance peak is visible as a shoulder. This is even more pronounced in the difference-PDFs (dPDFs) obtained by subtraction of the measurement at 20 °C (see SI Figure S1). At 345 °C the two peaks are located at 3.34 Å and 3.64 Å. One explanation for this splitting is the formation of differently connected NiO_6 octahedra, for example via different tilt angles of neighbouring octahedra (see Figure 3a inset). With XANES we could confirm, that the large majority of Ni atoms stays in the oxidation state Ni^{II} until 345 °C, as the white line and the pre-peak are showing only minor changes, (but with a clear trend towards reduced species) (see SI Fig. S2). The change of the Ni···Ni distance is due to tilted corner-shared NiO_6 octahedra, also

indicating a distortion in the framework with rising temperature. The increase of the pre-peak feature also supports this finding, as it hints towards a change of a symmetric to a less symmetric Ni^{II} environment.

The PXRDs show no change of space group symmetry (see SI Figure S3). This means that the structural transitions in the framework are mostly short-range order effects.

For further insights into the temperature-induced structural changes of Ni(BDC)(PNO), PDF and Rietveld refinements were conducted using the crystal structure of the isostructural Co(BDC)(PNO).[22] The lattice parameters *a*, *b*, *c* from the PDF refinements show nearly linear trends with temperature, where *a* is decreasing, *b* is nearly constant and *c* is increasing with temperature (see SI Figure S4). The lattice parameters *b* and *c* from the Rietveld refinements follow a similar trend but have a large error (see SI Figure S5). This is due to the low Q-resolution of the total scattering measurement setup with a small sample-detector-distance and the X-rays had a small wavelength, resulting in broad overlapped Bragg peaks (see SI Figure S6). The lattice parameter *a* shows no clear trend up to 300 °C, when it starts to decrease with a lower overall error value. The trend of lattice parameters leads to a rising angle δ between the BDC linkers (see Figure 1 and Figure 4). Such behaviour was also found by DeVries *et al.* for the HMOF-1.[44] To our knowledge, we are the first to report this on the Ni(BDC)(PNO), being a close relative of the MIL-53 framework. Overall, the unit cell volume *V* of the MOF is increasing linearly until 200 °C with a thermal expansion coefficient of $\alpha_V = 7.6 \cdot 10^{-5}\ K^{-1}$. Then, the cell volume plateaus and finally shrinks slowly due to the dominating decrease of the lattice parameter *a*. To account for finite size dampening in the PDF from crystallite size and amorphization, a parameter for the attenuated crystal spherical shape function, was used.[45] The refined domain size shows a decrease starting at 240 °C with an even stronger decrease beyond 315 °C, indicating an accelerated amorphization of the framework (SI Figure S7). This amorphization is induced by the release of the solvent dimethylformamide (DMF) used in the synthesis, which is trapped inside the MOF crystals. This solvent release is proven with TGA-MS, in which a m/z signal attributed to a DMF fragment is observed from 220 °C onwards (see SI Figure S12). The boiling point of DMF is 153 °C at 1 bar but the crystal prevents the release until enough pressure is built up in the pore. The pressure needed for DMF to boil at 220 °C is ca. 6 bar calculated with the Clausius-Clapeyron equation (see SI).

The goodness of fit parameter R_w of the PDF refinements worsens with increasing temperature. This leads to the conclusion, that structural changes occur that cannot be described by the Ni(BDC)(PNO) crystal structure. A comparison between the PDF refinements at 20 °C and 345 °C in He is shown in SI Figure S8.

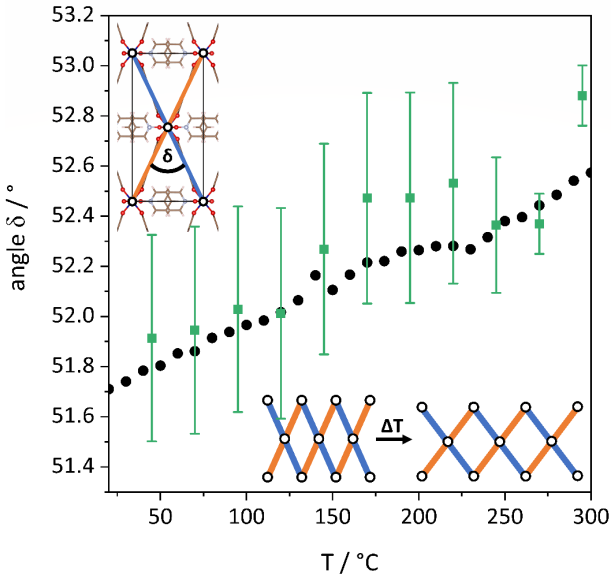

Figure 4: Distortion of the framework reflected in the angle δ of the BDC linker, calculated from the lattice parameters *a* and *c*. Values from Rietveld refinement are shown as green squares (with error bars) and values from PDF refinement are showns as black dots.

We observed that the refined PDF peaks of Ni(BDC)(PNO) at an elevated temperature of 245 °C in the range up to 5 Å were too broad and the refined peaks in the range 5-40 Å were too narrow (see SI Figure S9). This implies that the refined isotropic thermal displacement is too high and too low for the respective ranges. While the intramolecular distances have low relative displacement, the intermolecular distances have high displacements caused by the rotationional freedom of the benzene rings. Hence, separate refinements of the ranges 1-5 Å and 5-40 Å support this finding, as the B_{iso} for carbon at 245 °C is 0.3 Å^2 in the range 1-5 Å and and 4.1 Å^2 in the range 5-40 Å, respectively.

NMF mapping of the main components

Non-negative matrix factorization breaks down the whole PDF pattern into its components and proved to be a useful tool for *in-situ* experiments with multiple phases.[46,47] In the case of MOF decomposition, the main components are the MOF, the formed Ni nanoparticles and possibly secondary phases. From the NMF weights of these components, we can conclude the course of decomposition to further support the sequential PDF refinements. Thatcher *et al.* showed that the NMF weights are in good agreement with the molar phase fractions from Rietveld refinements.[46] The NMF mapping is also not dependent on any structural information, like a crystal structure, which is especially helpful in our case of amorphization of the framework and evolution of nanoparticles. To validate the significance of the NMF mapping, we compared the NMF weights with the molar contents found by sequential PDF refinements, which match well.

Further, the molar content of the MOF phase in the NMF mapping and PDF refinements is in line with the TGA experiments (see Figure 5). In order to compare the progress of

decomposition, the point where the NMF weight of the MOF was 50 % was taken as a benchmark point. Higher decomposition temperatures lead to faster decomposition. 50 % of the MOF was already decomposed for two heat ramps at ca. 395 °C (396 °C for 10H_2-411 and 393 °C for 10H_2-500 °C). This matches again well with the complementary TGA method, where 50% loss of organic linker occurred at 400 °C (for further information see SI). The decomposition atmosphere had a significant impact on the decomposition rate of the MOF. Without hydrogen as a reducing agent, 50 % decomposition occurred only at 418 °C. This can be explained by the reaction of the strong reducing agent H_2 with the organic linker, breaking the bonds between the central Ni^{II} and the oxygen of the organic linker, also leading to the reduction of Ni^{II} to Ni^0.

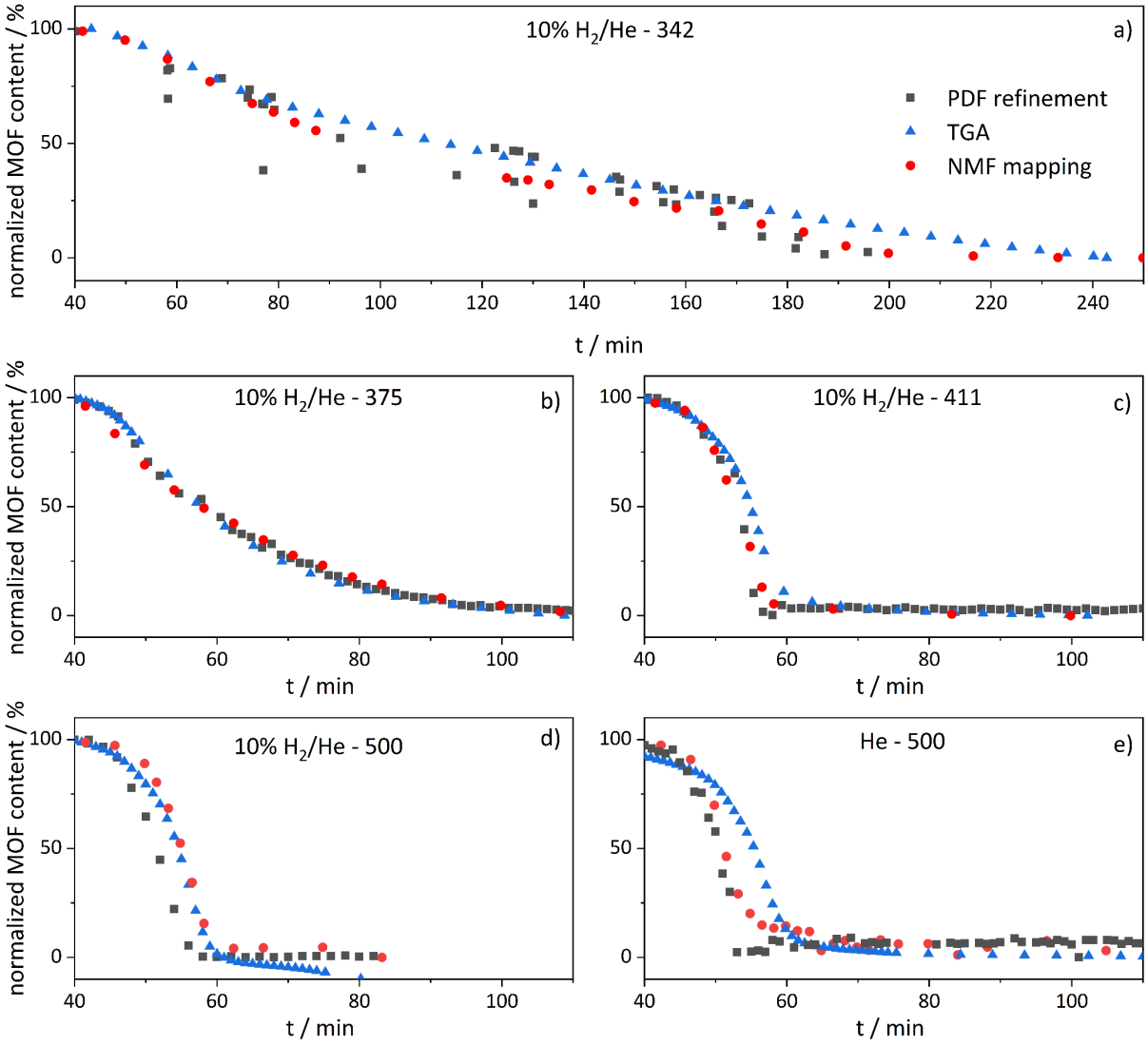

Figure 5: Comparison of the molar content resulting from PDF refinements (black square), TGA (blue triangle) and NMF mapping (red circle): a) 10H_2-342, b) 10H_2-375, c) 10H_2-411, d) 10H_2-500, e) He-500. Note that 10H_2-342 is shown over a larger timeframe.

***In-situ* X-ray scattering during the formation of the catalyst in reductive atmosphere**

In-situ PDF experiments during the formation of the catalyst were performed to track the nanoparticle growth and identify mechanistic steps during the decomposition of the MOF. Complementary TGA-MS and XANES experiments were conducted to correlate structural features with the decomposition process. Exemplary, the PDF experiment $10H_2$–375 is showcased. We confirmed the reproducibility of the experiments $10H_2$-342,375,411,500 by comparing the PDF refinements of the MOF up to 342 °C (see SI Figure S16). In 10% H_2/He the amorphization of the MOF starts at around 270 °C, visible in the peak broadening and the loss of intensity of peaks at higher distances (see Figure 6b). The peaks at 7.1 Å and 14.2 Å vanish representing a loss of crystallinity. TGA showed the first maximum in the derivative curve at 270 °C (see SI Figure S11), revealing that a mass loss coincides with the amorphization of the framework. As described earlier this is due to trapped DMF in the MOF crystals that damages the crystalline structure as soon as it is released as volatile components.

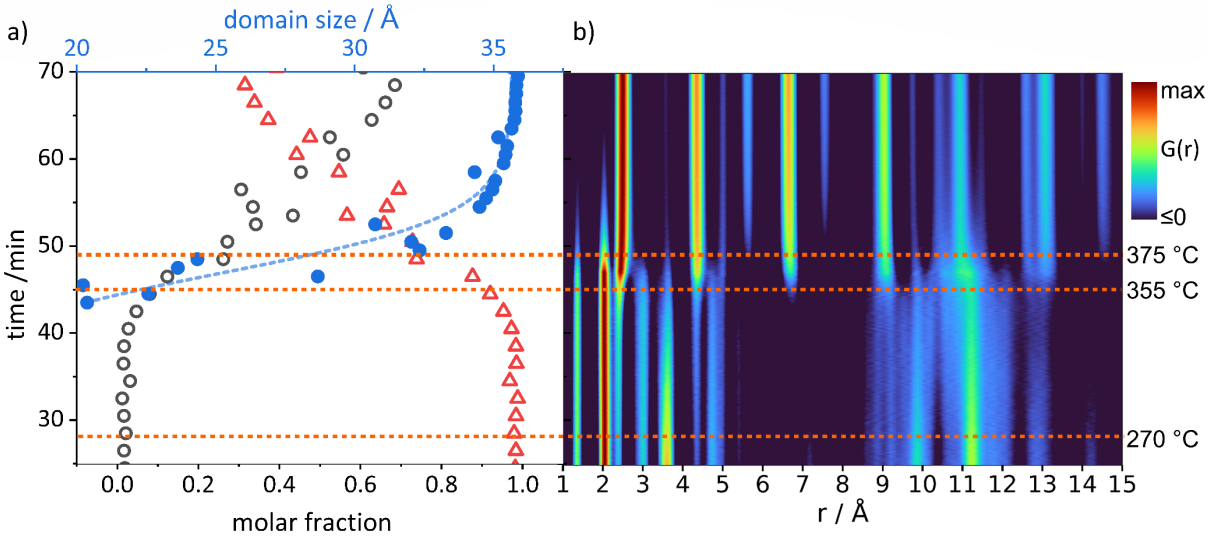

Figure 6: a) Molar fraction of Ni(BDC)(PNO) (red triangles) and Ni_{fcc} (black circles) and the corresponding domain size of the Ni_{fcc} phase from PDF refinements. The domain size was fitted with a Boltzmann curve (blue dashed line). b) Heatmap of *in-situ* PDF measurements of $10H_2$–375. The onset of amorphization at 270 °C, the start of nanoparticle formation at 355 °C and the final temperature are marked with dashed orange lines. The heatmap is normalized to the highest G(r) value and G(r) values ≤ 0 are set to the dark blue color for better visibility.

At around 355 °C, Ni nanoparticles start to form, featuring seven coordination shells within a measurement time of 10 s, i.e. the time resolution of the experiment, since Ni···Ni distances of a Ni_{fcc} structure appear up to 6.7 Å (see Figure 6b). The Ni···Ni distances of the first nanoparticles at 355 °C are elongated by 0.7% compared to bulk Ni (taking into account the thermal expansion coefficient of ca. $14 \cdot 10^{-6}$ K^{-1} and the lattice parameter 3.5238 Å for bulk Ni in the literature).[48,49] Furthermore, the peaks corresponding to the Ni nanoparticles are very broad (see SI Figure S18), especially for the higher coordination shells. This underlines the disordered nature of these nanoparticles. The sample becomes inhomogeneous with co-existing amorphous MOF and Ni_{fcc} phase. To shed more light onto the phase evolution, two-phase PDF refinements were carried out with a Ni_{fcc} and Ni(BDC)(PNO) phase in which the lattice

parameter, the molar content, the domain size and isotropic thermal displacement parameters were refined for each phase (see SI Table S3). The Ni(BDC)(PNO) molar content starts to decrease slowly at around 340 °C and the degradation was accelerated at 370 °C (see Figure 6a). At 370 °C, it was possible to reliably refine the first Ni nanoparticles with a domain size of ca. 20 Å.

Further, XANES indicates the first formation of Ni^0 nanoparticles by the shift of the edge position towards lower energies, thus indicating reduced species. The increasing intensity of the pre-peak at 355 °C shows the reduction of a fraction of Ni^{II} to metallic Ni^0 (see Figure 7), which is completed at 500 °C.

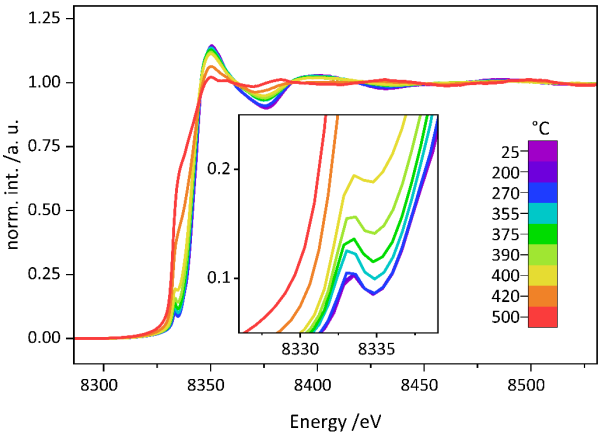

Figure 7: XANES spectra of 10H_2-500 at selected temperatures. The inset is a zoom into the pre-peak region.

According to TGA, at 355 °C the main mass loss starts to take place, see shoulder in derivative curve in Figure 8. The mass spectrum showed first a fragment at m/z = 79 belonging to pyridine and at higher temperatures a fragment at m/z = 78 belonging to benzene. Hence, the PNO linker is released from the framework first followed by the BDC linker at higher temperatures. This is also visible in the PDFs in the intensities of the C-C and Ni···N distances in the temperature range 365-410 °C (see SI Figure S17). The intensity of Ni···N, stemming from Ni···PNO interaction, is decreasing much faster, than the intensity from C-C, stemming from PNO and BDC intramolecular distances. Further, reduced benzene species like cyclohexene and cyclohexane could be observed in TGA-MS, showing that reduction of the organic linkers took place (SI Figure S12).

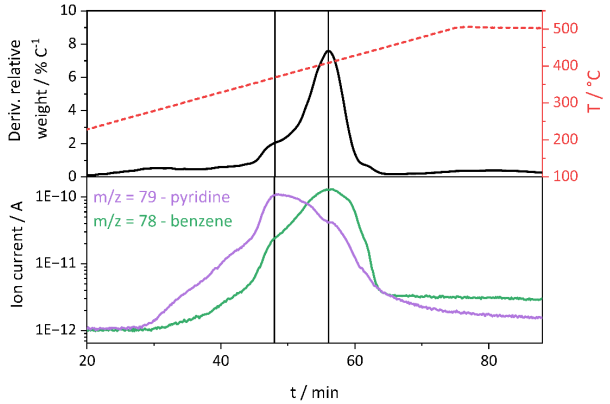

Figure 8: TGA-MS of $10H_2$-500 with derivative relative weight curve (top) and corresponding MS signal for pyridine and benzene (bottom).

After initial formation, the nanoparticles grow quickly to a domain size of 35 Å upon reaching the final temperature of 375°C, at which they remain stable, at least for more than two hours under thermal treatment conditions. At the end of the decomposition experiments, besides the Ni_{fcc} phase, a small signal of graphitic carbon remains in the PXRD (see SI Figure S19), underlining the conversion of the organic linker to a stabilizing carbon matrix, which we identified based on TEM investigations before.[21]

With XANES the nanoparticle growth and a change of Ni^0/N^{II} ratio are visible in the increase of the pre-peak up to 400 °C together with a shift of E_0 to lower energies in Figure 7. The white line intensity decreases while the intensity of the first oscillation increases. This is typical for samples with high elemental metal content, as the lighter backscatterers in the direct coordination environment of the MOF are replaced by heavier backscatterers in the nanoparticles. At higher temperatures, the pre-peak and edge are not distinguishable, which is typical for metallic species.[50] At 500 °C the edge is at 8333 eV, the value for Ni^0, which indicates the complete reduction of Ni species.[51]

The TGA of $10H_2$–375 and $10H_2$–500 showed a distinctive difference in the relative mass loss curves and their derivatives, see SI Figure S15. The mass loss attributed to the framework decomposition starts for both at 355 °C and proceeds in the same manner up to 375 °C: From there on, the mass loss in $10H_2$–500 is accelerated, visible in a maximum in the derivative curve at 400 °C and the framework decomposition is finished at ca. 420 °C. The mass loss for $10H_2$–375 is decelerated after reaching 375 °C and approaches the same relative weight of 28 % after a longer holding time (see SI Fig. S16). For $10H_2$-500 a second decomposition step after 420 °C is visible in the TGA. The m/z signal coinciding with this mass loss belongs to CH_4 (see SI Figure S13), which could evolve *via* hydrogenation of carbon that is surrounding the Ni nanoparticles.

XANES of the samples with longer time on stream at 500 °C showed that the two features in the white line swap intensity (see SI Figure S20 inset). Thus, at the beginning, the direct white line feature (around 8350 eV) is higher than the neighboring one (around 8357 eV), which represents a mixing of the backscattered radiation of the nearest neighbors. With increasing holding time, the intensity of the first white line feature (8350 eV) becomes lower than the first oscillation (around 8357 eV). This indicates that lighter components such as carbon or oxygen are being removed from

the sample and the sample is becoming more metallic which could be an indication of nanoparticle growth. This poses a problem to the stability of the nanoparticles when the thermal treatment at high temperatures is executed longer.

The domain sizes and their growth varied significantly between the different end temperatures. For $10H_2$-411 and 500, we observed fast nanoparticle growth within 45-55 minutes until a stable particle size was reached (see Figure 9a). For $10H_2$-375, the particle growth is slowing down at 50 minutes, which can be explained by the slower framework decomposition detected by TGA, NMF and PDF (see Figure 5). For $10H_2$-342, the domain size growth is even slower from the very beginning, and did not enter a plateau after 80 min, well in line with the TGA results. The scattering of data points in the curves could stem from the movement of the powder in the capillary during decomposition when gases were released.

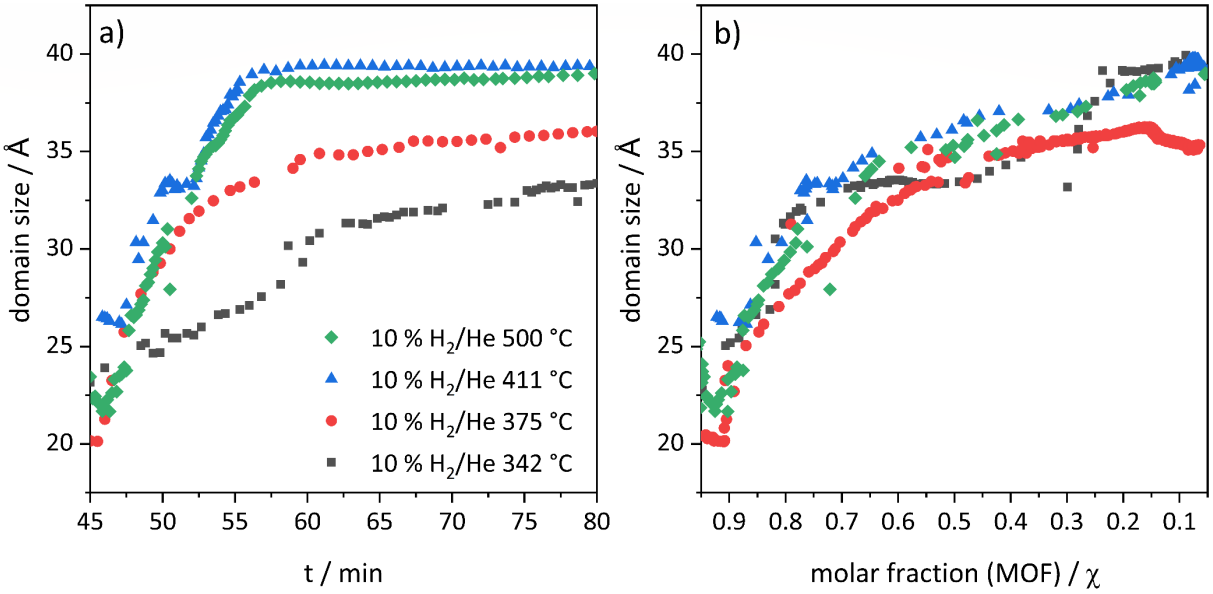

Figure 9: Refined domain size of $10H_2$–342 (black squares), 375 (red dots), 411 (blue triangles), and 500 (green diamonds) a) plotted versus time and b) plotted versus the molar fraction of the MOF.

We used the refined molar content of the MOF (see SI Figure S21) to check the dependence of Ni_{fcc} domain sizes on the degree of decomposition, by plotting the domain sizes vs. the molar content, see Figure 9b. The domain sizes follow a similar trend of growth independent of the end temperature, but mostly dependent on the degree of decomposition. This means, that the domain size can mainly be controlled by the holding time at the specific temperature. Overall, the mechanism of decomposition and formation of nanoparticles was comparable for different temperatures.

***In-situ* total scattering during the formation of the catalyst in non-reductive atmosphere**

In He atmosphere, the decomposition follows a different pathway than in the reductive one. In He, the amorphization of the MOF starts around 275 °C and the first nanoparticle formation is visible at 360 °C, which is 5 °C higher than in reductive atmosphere. This was confirmed by TGA, where the mass loss is observed at ca. 10 °C

higher temperature under inert conditions (see SI Figure S14). TGA-MS revealed additionally, that no reduced aromatics like cyclohexene and cyclohexane were released during the decomposition in non-reductive atmosphere. The second decomposition step present in reductive atmosphere, during which carbon is hydrogenated to CH_4, is also missing in He. Further, a side phase appeared at 410 °C that persisted even upon reaching the end temperature 500 °C after 74 min, see Fig. 9b. The NMF mapping also detected one side phase, which could be assigned to NiO (see SI Figure S22).

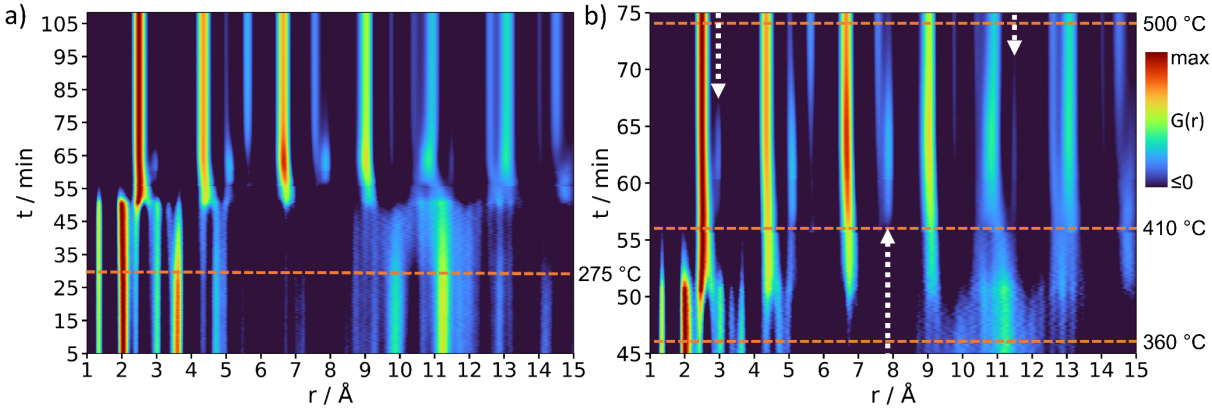

Figure 10: a) *In-situ* PDF heatmap of He–500. b) Zoom into the region 45-75 minutes (corresponding to 350-500 °C). Key temperatures are showcased by dashed orange lines. The formation of the side phase is marked with dashed white arrows.

In order to identify the crystalline side phases, we indexed the PXRD patterns and found not only one side phase already visible in the PDFs, but two side phases that formed consecutively (see SI Figure S23). The first phase formed is a hexagonal phase, which could either be Ni_3C or Ni_{hcp}. Ni_3C and Ni_{hcp} are difficult to distinguish because Ni_3C is isostructural to Ni_{hcp} with carbon on interstitial sites of the hexagonal lattice.[39] The identified hexagonal side phase matches the reference measurement of a synthesized Ni_3C. Since Ni_{fcc} is known to form metastable hexagonal phases by the introduction of lighter elements on interstitial sites, we propose that initially Ni_3C is formed given the large carbon content in our sample.[52] The scattering power of C is very low compared to Ni, which results in identical PXRD patterns with a slightly larger lattice parameter for Ni_3C compared to Ni_{hcp}.

The second phase can be attributed to cubic NiO, which is formed by the oxygen-rich organic linker. In reductive atmosphere, the formation of NiO was suppressed by the addition of H_2. The decomposed organics, that formed the carbon residuals are able to reduce NiO, which happens at higher temperatures and leads to the conversion of NiO to Ni_{fcc} in non-reductive atmosphere.

To quantify these qualitative observations, sequential four-phase PDF refinements with Ni(BDC)(PNO) (CCDC entry 947945), Ni_{fcc} (ICSD entry 111370), Ni_{hcp} (ICSD entry 76668) and NiO (ICSD entry 131090) crystal structures starting at 305 °C were done (see Figure 11 a). The Ni(BDC)(PNO) phase was removed from the refinement when it approached zero at 55 min. The refined relative molar content shows a steep rise of Ni_{fcc} in the 360 – 430 °C regime and afterward a continuous rise up to 80 % at 500 °C. The hexagonal

Ni phase starts to form at 370 °C and has a maximum of 40 % at 405 °C. It then decreases back to around 10% transforming either to Ni_{fcc} or NiO. The NiO molar phase content starts rising at 405 °C to a maximum at 455 °C and then decreases to <10% at 500 °C.

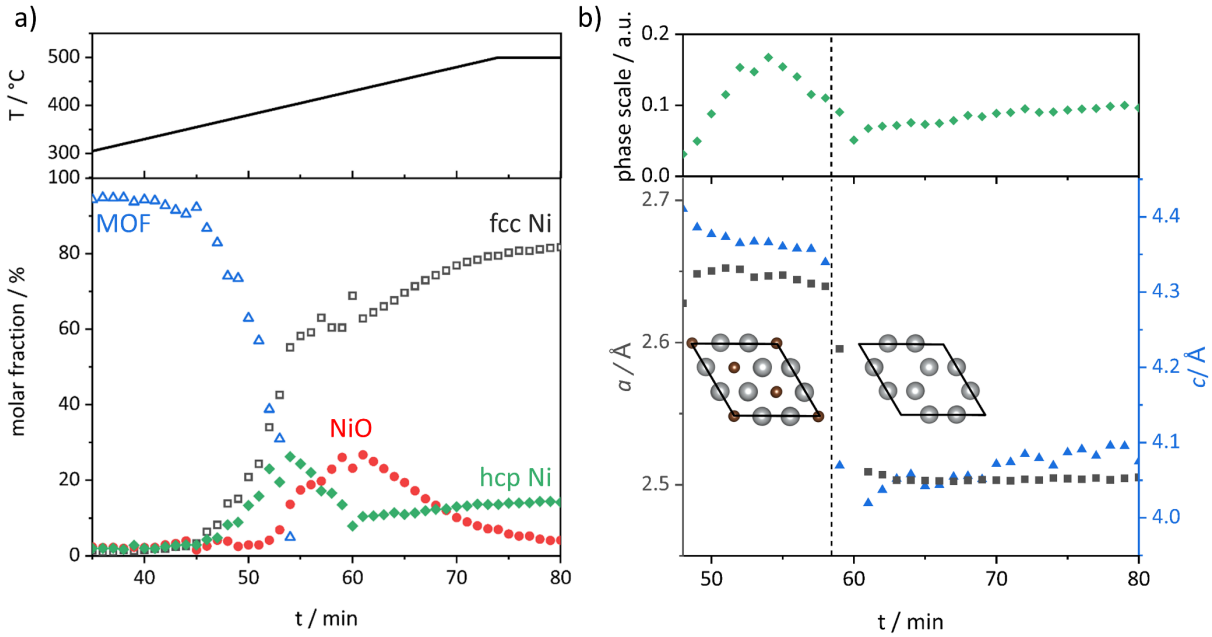

Figure 11: a) Evolution of molar phase fractions during four-phase (up to 54 min) and three-phase (after 55 min) sequential PDF refinements of He–500 °C. Ni(BDC)(PNO) (open blue triangles), Ni_{fcc} (open black squares), Ni_3C (green diamonds) and NiO (red dots) structures were refined. The Ni(BDC)(PNO) structure was removed from the refinement when it approached zero at 55 min. The temperature ramp is shown above. b) Lattice parameters *a* (black squares) and *c* (blue triangles) of the refined hexagonal phase are displayed, together with the phase scale of Ni_{hcp}. The jump of the lattice parameter is visualized by the lattices of Ni_3C (left) and Ni_{hcp} (right).

The Ni_{hcp} lattice parameters were also refined and showed a significant drop at 450 °C (see Figure 11 b), coinciding with the drop of the the molar content of the hexagonal phase. This can be attributed to a partial phase transformation from Ni_3C to Ni_{hcp}, as the carbon is leaving the interstitial sites of the hexagonal lattice, which contracts the lattice parameters *a* and *c* from 2.673 and 4.363 Å to 2.504 and 4.058 Å, respectively.[53] In our previous work, we observed a hexagonal phase in the pre-catalyst with *ex-situ* X-ray scattering.[21] With this *in-situ* study, we can now demonstrate that Ni_3C is formed in presence of carbon and under inert atmosphere at temperatures around 370 °C. It is then further converted to Ni_{hcp} at higher temperatures of 450 °C.

Conclusions

With *in-situ* PDF and XANES experiments we elucidated mechanistic details of the thermal decomposition of the Ni(BDC)(PNO) MOF, leading to active CO_2 methanation catalysts. The MOF structure is structurally stable up to ca. 170 °C and higher temperatures lead to more rotational freedom of the benzene ring of the BDC linker. Further heating triggers a structural transformation, where the Ni-O distance contracts

and the NiO_6 octahedra tilt. At 240 °C this distortion begins to disturb the crystalline long-range order leading to amorphization. Additionally, TGA-MS showed that DMF is trapped inside the MOF and is released, correlating with amorphization.
Besides the temperature-induced changes of Ni(BDC)(PNO), we studied the influence of the atmosphere (He vs. 10% H_2/He) and thermal treatment temperature on the course of the decomposition.
Under reductive atmosphere, small Ni nanoparticles form at around 355 °C, which rapidly grow until a stable domain size of 35-40 Å is reached. From the parameters investigated, the domain size growth only depends on the degradation degree of the MOF, which is influenced by the gas atmosphere and holding time at the chosen temperatures. TGA-MS shows that the decomposition of the framework starts with PNO leaving the framework, followed by the BDC linker at higher temperatures or longer holding times. A fraction of graphitic carbon is visible in the PXRD after each decomposition experiment ($10H_2$-342, 375, 411, 500 and He–500), leading to the conclusion, that the nanoparticles are stabilized in a carbon matrix as previously observed in TEM. Under reductive atmosphere and higher temperature, further decomposition of this carbon shell was observed with TGA-MS.
The decomposition in non-reductive He atmosphere proceeds with the formation of two different hexagonal Ni side phases and a cubic NiO side phase. The first hexagonal phase forms at 370 °C by intercalation of carbon into the Ni lattice to yield Ni_3C. At higher temperatures the carbon leaves the interstitial atom sites, reflected in the jump in the lattice parameter of the hexagonal phase. A metastable Ni_{hcp} evolves, which partly transitions to the stable Ni_{fcc} phase. A small Ni_{hcp} fraction remains until the end of the decomposition process, possibly stabilized by the surrounding carbon. The NiO phase, which forms at 405 °C by the oxygen-rich organic linker, disappears almost entirely after reaching 500 °C.
From these *in-situ* PDF and XANES experiments we conclude, that for the formation of a MOF-derived Ni@C methanation catalyst, a reducing atmosphere is needed to obtain a single phase product. The decomposition temperature plays a crucial role in the process, as high temperatures lead to further undesired decomposition of the stabilizing carbon matrix. Most synthetic procedures for MOF-derived catalysts in the literature were done under inert atmosphere, only.[54] The use of a reductive atmosphere could pose an optimization for further rational catalyst and material design.

Conflicts of interest

There are no conflicts to declare.

Acknowledgements

We acknowledge funding by the Deutsche Forschungsgemeinschaft (DFG, German Research Foundation) via SPP2080 (BA 4467/8-1 and BA 4467/8-2, ZO 369/2-1 and ZO

369/2-2). We thank Wolfgang Kleist and Leif Rohrbach (TU Kaiserslautern) for providing the initial MOFs. We acknowledge DESY (Hamburg, Germany), a member of the Helmholtz Association HGF, for provision of experimental facilities, with research carried out at PETRA III using beamlines P21.1 and P65, proposal I-20190332 and I-20190950. We gratefully acknowledge Ann-Christin Dippel and Edmund Welter for support during the beamtime, as well as Mirco Eckardt, Sabrina Thomä and Leif Rohrbach. We thank Jasmin Allan and Andrey Tarasov from the workgroup of Thomas Lunkenbein (FHI Berlin) for the TGA-MS measurements. We thank Malte Grunert for discussion and help with python-based data processing.

References

1 L. Oar-Arteta, T. Wezendonk, X. Sun, F. Kapteijn and J. Gascon, Metal organic frameworks as precursors for the manufacture of advanced catalytic materials, *Mater. Chem. Front.*, 2017, **1**, 1709–1745. DOI: 10.1039/C7QM00007C.

2 S. Dang, Q.-L. Zhu and Q. Xu, Nanomaterials derived from metal–organic frameworks, *Nat Rev Mater*, 2018, **3**. DOI: 10.1038/natrevmats.2017.75.

3 J. Zhang, B. An, Y. Hong, Y. Meng, X. Hu, C. Wang, J. Lin, W. Lin and Y. Wang, Pyrolysis of metal–organic frameworks to hierarchical porous Cu/Zn-nanoparticle@carbon materials for efficient CO 2 hydrogenation, *Mater. Chem. Front.*, 2017, **1**, 2405–2409. DOI: 10.1039/c7qm00328e.

4 K. Nakatsuka, T. Yoshii, Y. Kuwahara, K. Mori and H. Yamashita, Controlled Pyrolysis of Ni-MOF-74 as a Promising Precursor for the Creation of Highly Active Ni Nanocatalysts in Size-Selective Hydrogenation, *Chemistry*, 2018, **24**, 898–905. DOI: 10.1002/chem.201704341.

5 R. Wu, D. P. Wang, X. Rui, B. Liu, K. Zhou, A. W. K. Law, Q. Yan, J. Wei and Z. Chen, In-situ formation of hollow hybrids composed of cobalt sulfides embedded within porous carbon polyhedra/carbon nanotubes for high-performance lithium-ion batteries, *Advanced materials (Deerfield Beach, Fla.)*, 2015, **27**, 3038–3044. DOI: 10.1002/adma.201500783.

6 Z.-F. Huang, J. Song, K. Li, M. Tahir, Y.-T. Wang, L. Pan, L. Wang, X. Zhang and J.-J. Zou, Hollow Cobalt-Based Bimetallic Sulfide Polyhedra for Efficient All-pH-Value Electrochemical and Photocatalytic Hydrogen Evolution, *J. Am. Chem. Soc.*, 2016, **138**, 1359–1365. DOI: 10.1021/jacs.5b11986.

7 B. Y. Xia, Y. Yan, N. Li, H. B. Wu, X. W. Lou and X. Wang, A metal–organic framework-derived bifunctional oxygen electrocatalyst, *Nat Energy*, 2016, **1**. DOI: 10.1038/nenergy.2015.6.

8 H. Zhu, J. Zhang, R. Yanzhang, M. Du, Q. Wang, G. Gao, J. Wu, G. Wu, M. Zhang, B. Liu, J. Yao and X. Zhang, When cubic cobalt sulfide meets layered molybdenum disulfide: a core-shell system toward synergetic electrocatalytic water splitting, *Advanced materials (Deerfield Beach, Fla.)*, 2015, **27**, 4752–4759. DOI: 10.1002/adma.201501969.

9 J. Zhu, Z. Xu and B. Lu, Ultrafine Au nanoparticles decorated NiCo2O4 nanotubes as anode material for high-performance supercapacitor and lithium-ion battery applications, *Nano Energy*, 2014, **7**, 114–123. DOI: 10.1016/j.nanoen.2014.04.010.

10 K. Mori, K. Miyawaki and H. Yamashita, Ru and Ru–Ni Nanoparticles on TiO 2 Support as Extremely Active Catalysts for Hydrogen Production from Ammonia–Borane, *ACS Catal.*, 2016, **6**, 3128–3135. DOI: 10.1021/acscatal.6b00715.
11 J. Li, W. Li, G. Liu, Y. Deng, J. Yang and Y. Chen, Tricobalt tetraoxide-supported palladium catalyst derived from metal organic frameworks for complete benzene oxidation, *Catal Lett*, 2016, **146**, 1300–1308. DOI: 10.1007/s10562-016-1753-2.
12 J. Kim, G. T. Neumann, N. D. McNamara and J. C. Hicks, Exceptional control of carbon-supported transition metal nanoparticles using metal-organic frameworks, *J. Mater. Chem. A*, 2014, **2**, 14014. DOI: 10.1039/c4ta03050h.
13 Y. Kimitsuka, E. Hosono, S. Ueno, H. Zhou and S. Fujihara, Fabrication of porous cubic architecture of ZnO using Zn-terephthalate MOFs with characteristic microstructures, *Inorg. Chem.*, 2013, **52**, 14028–14033. DOI: 10.1021/ic4017849.
14 Z. Long, L. Wei, L. Shuang, W. Jifei, W. Huanlei and C. Jiaxin, Fe 3 O 4 nanoplates/carbon network synthesized by in situ pyrolysis of an organic–inorganic layered hybrid as a high-performance lithium-ion battery anode, *J. Mater. Chem. A*, 2015, **3**, 14210–14216. DOI: 10.1039/c5ta01926e.
15 B. Liu, H. Shioyama, T. Akita and Q. Xu, Metal-organic framework as a template for porous carbon synthesis, *J. Am. Chem. Soc.*, 2008, **130**, 5390–5391. DOI: 10.1021/ja7106146.
16 T. Kundu, S. C. Sahoo and R. Banerjee, Solid-State Thermolysis of Anion Induced Metal–Organic Frameworks to ZnO Microparticles with Predefined Morphologies: Facile Synthesis and Solar Cell Studies, *Cryst. Growth Des.*, 2012, **12**, 2572–2578. DOI: 10.1021/cg300174f.
17 B. Liu, X. Zhang, H. Shioyama, T. Mukai, T. Sakai and Q. Xu, Converting cobalt oxide subunits in cobalt metal-organic framework into agglomerated Co3O4 nanoparticles as an electrode material for lithium ion battery, *Journal of Power Sources*, 2010, **195**, 857–861. DOI: 10.1016/j.jpowsour.2009.08.058.
18 R. Lippi, S. C. Howard, H. Barron, C. D. Easton, I. C. Madsen, L. J. Waddington, C. Vogt, M. R. Hill, C. J. Sumby, C. J. Doonan and D. F. Kennedy, Highly active catalyst for CO 2 methanation derived from a metal organic framework template, *J. Mater. Chem. A*, 2017, **5**, 12990–12997. DOI: 10.1039/c7ta00958e.
19 V. P. Santos, T. A. Wezendonk, J. J. D. Jaén, A. I. Dugulan, M. A. Nasalevich, H.-U. Islam, A. Chojecki, S. Sartipi, X. Sun, A. A. Hakeem, A. C. J. Koeken, M. Ruitenbeek, T. Davidian, G. R. Meima, G. Sankar, F. Kapteijn, M. Makkee and J. Gascon, Metal organic framework-mediated synthesis of highly active and stable Fischer-Tropsch catalysts, *Nature communications*, 2015, **6**, 6451. DOI: 10.1038/ncomms7451.
20 Z. Tao, T. Wang, X. Wang, J. Zheng and X. Li, MOF-Derived Noble Metal Free Catalysts for Electrochemical Water Splitting, *ACS applied materials & interfaces*, 2016, **8**, 35390–35397. DOI: 10.1021/acsami.6b13411.
21 N. Prinz, L. Schwensow, S. Wendholt, A. Jentys, M. Bauer, W. Kleist and M. Zobel, Hard X-ray-based techniques for structural investigations of CO2 methanation catalysts prepared by MOF decomposition, *Nanoscale*, 2020, **12**, 15800–15813. DOI: 10.1039/d0nr01750g.
22 A. S. Munn, G. J. Clarkson, F. Millange, Y. Dumont and R. I. Walton, M(ii) (M = Mn, Co, Ni) variants of the MIL-53-type structure with pyridine-N-oxide as a co-ligand, *CrystEngComm*, 2013, **15**, 9679. DOI: 10.1039/c3ce41268g.

23 S. J. L. Billinge and M. G. Kanatzidis, Beyond crystallography: the study of disorder, nanocrystallinity and crystallographically challenged materials with pair distribution functions, *Chem. Commun. (Cambridge, U. K.)*, 2004, 749–760. DOI: 10.1039/b309577k.
24 M. A. Newton, K. W. Chapman, D. Thompsett and P. J. Chupas, Chasing changing nanoparticles with time-resolved pair distribution function methods, *J. Am. Chem. Soc.*, 2012, **134**, 5036–5039. DOI: 10.1021/ja2114163.
25 M. Newton, Time Resolved Operando X-ray Techniques in Catalysis, a Case Study: CO Oxidation by O2 over Pt Surfaces and Alumina Supported Pt Catalysts, *Catalysts*, 2017, **7**, 58. DOI: 10.3390/catal7020058.
26 A. E. Platero-Prats, Z. Li, L. C. Gallington, A. W. Peters, J. T. Hupp, O. K. Farha and K. W. Chapman, Addressing the characterisation challenge to understand catalysis in MOFs: the case of nanoscale Cu supported in NU-1000, *Faraday discussions*, 2017, **201**, 337–350. DOI: 10.1039/c7fd00110j.
27 M. W. Terban, D. Banerjee, S. Ghose, B. Medasani, A. Shukla, B. A. Legg, Y. Zhou, Z. Zhu, M. L. Sushko, J. J. de Yoreo, J. Liu, P. K. Thallapally and S. J. L. Billinge, Early stage structural development of prototypical zeolitic imidazolate framework (ZIF) in solution, *Nanoscale*, 2018, **10**, 4291–4300. DOI: 10.1039/c7nr07949d.
28 H. Xu, S. Sommer, N. L. N. Broge, J. Gao and B. B. Iversen, The Chemistry of Nucleation: In Situ Pair Distribution Function Analysis of Secondary Building Units During UiO-66 MOF Formation, *Chem. - Eur. J.*, 2019, **25**, 2051–2058. DOI: 10.1002/chem.201805024.
29 M. Folkjær, L. F. Lundegaard, H. S. Jeppesen, M. J. Marks, M. S. Hvid, S. Frank, G. Cibin and N. Lock, Pyrolysis of a metal-organic framework followed by in situ X-ray absorption spectroscopy, powder diffraction and pair distribution function analysis, *Dalton Trans.*, 2022, **51**, 10740–10750. DOI: 10.1039/D2DT00616B.
30 Z. Chen, Z. Chen, O. K. Farha and K. W. Chapman, Mechanistic Insights into Nanoparticle Formation from Bimetallic Metal-Organic Frameworks, *J. Am. Chem. Soc.*, 2021, **143**, 8976–8980. DOI: 10.1021/jacs.1c04269.
31 M. A. Gotthardt, R. Schoch, S. Wolf, M. Bauer and W. Kleist, Synthesis and characterization of bimetallic metal-organic framework Cu-Ru-BTC with HKUST-1 structure, *Dalton Trans.*, 2015, **44**, 2052–2056. DOI: 10.1039/c4dt02491e.
32 S. Schuster, E. Klemm and M. Bauer, The role of Pd2+/Pd0 in hydrogenation by Pd(2-pymo)2n: an X-ray absorption and IR spectroscopic study, *Chem. - Eur. J.*, 2012, **18**, 15831–15837. DOI: 10.1002/chem.201202129.
33 M. Bauer and H. Bertagnolli, in *Methods in Physical Chemistry*, ed. R. Schäfer and P. C. Schmidt, Wiley-VCH, Weinheim, 2nd edn., 2012, pp. 231–269.
34 M. Xing, J. Mohapatra, F. Zeng and J. Ping Liu, Magnetic properties of nickel carbide nanoparticles with enhanced coercivity, *AIP Advances*, 2018, **8**, 56308. DOI: 10.1063/1.5006350.
35 C. J. Wright and X. D. Zhou, Computer-assisted area detector masking, *J. Synchrotron Radiat.*, 2017, **24**, 506–508. DOI: 10.1107/S1600577517000157.
36 P. Juhás, T. Davis, C. L. Farrow and S. J. L. Billinge, PDFgetX3 : a rapid and highly automatable program for processing powder diffraction data into total scattering pair distribution functions, *J. Appl. Crystallogr.*, 2013, **46**, 560–566. DOI: 10.1107/S0021889813005190.

37 P. Juhás, C. L. Farrow, X. Yang, K. R. Knox and S. J. L. Billinge, Complex modeling: a strategy and software program for combining multiple information sources to solve ill posed structure and nanostructure inverse problems, *Acta Crystallogr., Sect. A: Found. Adv.*, 2015, **71**, 562–568. DOI: 10.1107/S2053273315014473.
38 B. Ravel and M. Newville, ATHENA, ARTEMIS, HEPHAESTUS: data analysis for X-ray absorption spectroscopy using IFEFFIT, *J. Synchrotron Radiat.*, 2005, **12**, 537–541. DOI: 10.1107/S0909049505012719.
39 M. Newville, IFEFFIT: interactive XAFS analysis and FEFF fitting, *J. Synchrotron Radiat.*, 2001, **8**, 322–324. DOI: 10.1107/s0909049500016964.
40 T. S. Ertel, H. Bertagnolli, S. Hückmann, U. Kolb and D. Peter, XAFS Spectroscopy of Liquid and Amorphous Systems: Presentation and Verification of a Newly Developed Program Package, *Appl. Spectrosc.*, 1992, **46**, 690–698. DOI: 10.1366/0003702924125069.
41 N. Binsted and S. S. Hasnain, State-of-the-Art Analysis of Whole X-ray Absorption Spectra, *J. Synchrotron Radiat.*, 1996, **3**, 185–196. DOI: 10.1107/S0909049596005651.
42 D. I. Kolokolov, A. G. Stepanov and H. Jobic, Guest Controlled Rotational Dynamics of Terephthalate Phenylenes in Metal–Organic Framework MIL-53(Al): Effect of Different Xylene Loadings, *J. Phys. Chem. C*, 2014, **118**, 15978–15984. DOI: 10.1021/jp506010p.
43 A. Gonzalez-Nelson, F.-X. Coudert and M. A. van der Veen, Rotational Dynamics of Linkers in Metal¯Organic Frameworks, *Nanomaterials (Basel, Switzerland)*, 2019, **9**. DOI: 10.3390/nano9030330.
44 L. D. DeVries, P. M. Barron, E. P. Hurley, C. Hu and W. Choe, "Nanoscale lattice fence" in a metal-organic framework: interplay between hinged topology and highly anisotropic thermal response, *J. Am. Chem. Soc.*, 2011, **133**, 14848–14851. DOI: 10.1021/ja2032822.
45 K. Kodama, S. Iikubo, T. Taguchi and S. I. Shamoto, Finite size effects of nanoparticles on the atomic pair distribution functions, *Acta crystallographica. Section A, Foundations of crystallography*, 2006, **62**, 444–453. DOI: 10.1107/S0108767306034635.
46 Z. Thatcher, C. H. Liu, L. Yang, B. C. McBride, G. Thinh Tran, A. Wustrow, M. A. Karlsen, J. R. Neilson, D. B. Ravnsbæk and S. J. L. Billinge, nmfMapping: a cloud-based web application for non-negative matrix factorization of powder diffraction and pair distribution function datasets, *Acta Crystallogr., Sect. A: Found. Adv.*, 2022, **78**, 242–248. DOI: 10.1107/S2053273322002522.
47 C.-H. Liu, C. J. Wright, R. Gu, S. Bandi, A. Wustrow, P. K. Todd, D. O'Nolan, M. L. Beauvais, J. R. Neilson, P. J. Chupas, K. W. Chapman and S. J. L. Billinge, Validation of non-negative matrix factorization for rapid assessment of large sets of atomic pair distribution function data, *J. Appl. Crystallogr.*, 2021, **54**, 768–775. DOI: 10.1107/S160057672100265X.
48 P. Hidnert, Thermal Expansion of Some Nickel Alloys, *Journal of Research of the National Bureau of Standards*, 1957, **58**, 89–92.
49 P. Juhás, J. N. Louwen, L. van Eijck, E. T. C. Vogt and S. J. L. Billinge, PDFgetN3 : atomic pair distribution functions from neutron powder diffraction data using ad hoc corrections, *J. Appl. Crystallogr.*, 2018, **51**, 1492–1497. DOI: 10.1107/S1600576718010002.
50 R. Schoch, W. Desens, T. Werner and M. Bauer, X-ray spectroscopic verification of the active species in iron-catalyzed cross-coupling reactions, *Chem. - Eur. J.*, 2013, **19**, 15816–15821. DOI: 10.1002/chem.201303340.

51 J. Wang, A. Gili, M. Grünbacher, S. Praetz, J. D. Epping, O. Görke, G. Schuck, S. Penner, C. Schlesiger, R. Schomäcker, A. Gurlo and M. F. Bekheet, Silicon oxycarbonitride ceramic containing nickel nanoparticles: from design to catalytic application, *Mater. Adv.*, 2021, **2**, 1715–1730. DOI: 10.1039/d0ma00917b.
52 Z. L. Schaefer, K. M. Weeber, R. Misra, P. Schiffer and R. E. Schaak, Bridging hcp-Ni and Ni 3 C via a Ni 3 C 1- x Solid Solution: Tunable Composition and Magnetism in Colloidal Nickel Carbide Nanoparticles, *Chem. Mater.*, 2011, **23**, 2475–2480. DOI: 10.1021/cm200410s.
53 R.-T. Chiang, R.-K. Chiang and F.-S. Shieu, Emergence of interstitial-atom-free HCP nickel phase during the thermal decomposition of Ni3C nanoparticles, *RSC Adv.*, 2014, **4**, 19488. DOI: 10.1039/c4ra01874e.
54 T. Sun, L. Xu, D. Wang and Y. Li, Metal organic frameworks derived single atom catalysts for electrocatalytic energy conversion, *Nano Res.*, 2019, **12**, 2067–2080. DOI: 10.1007/s12274-019-2345-4.